

# Investigating the OH-H<sub>2</sub> relation in diffuse Galactic clouds

Katherine Rawlins<sup>1\*</sup> and Bhaswati Mookerjee<sup>2†</sup>

<sup>1</sup>*Department of Physics, St. Xavier's College, 5, Mahapalika Marg, Mumbai 400001, India*

<sup>2</sup>*Department of Astronomy & Astrophysics, Tata Institute of Fundamental Research, Homi Bhabha Road, Mumbai 400005, India*

Accepted XXX. Received YYY; in original form ZZZ

## ABSTRACT

We investigate the correlation between OH and H<sub>2</sub> column densities in diffuse Galactic clouds, in order to identify potential molecular tracers of interstellar H<sub>2</sub>. For this, we analyse near-UV spectra extracted from the ESO/VLT archives towards seventeen sightlines (five of them new) with known  $N(\text{H}_2)$ , along with nine sightlines with no H<sub>2</sub> information.  $N(\text{OH})$  shows only marginal correlation with  $N(\text{H}_2)$  ( $10^{20}$  to  $2 \times 10^{21}$  cm<sup>-2</sup>), at the 95 per cent confidence level. We use orthogonal distance regression analysis to obtain  $N(\text{OH})/N(\text{H}_2) = (1.32 \pm 0.15) \times 10^{-7}$ , which is  $\sim 33$  per cent higher than the previous estimates based on near-UV data. We also obtain  $N(\text{CH})/N(\text{H}_2) = (3.83 \pm 0.23) \times 10^{-8}$  and a significant correlation between  $N(\text{OH})$  and  $N(\text{CH})$ , with  $N(\text{OH}) = (2.61 \pm 0.19) \times N(\text{CH})$ , both of which are consistent with previous results. Comparison with predictions of numerical models indicate that OH absorption arises from diffuse gas ( $n_{\text{H}} \sim 50$  cm<sup>-3</sup>) illuminated by radiation fields  $\sim 0.5$ – $5$  G<sub>0</sub>, while CH is associated with higher density of 500 cm<sup>-3</sup>. We posit that the apparent dichotomy in the properties of the diffuse clouds giving rise to OH and CH absorption could be due to either (a) the presence of multiple spectroscopically unresolved clouds along the line-of-sight, or, (b) density gradients along the line-of-sight within a single cloud.

**Key words:** ISM: molecules – astrochemistry – ISM: photodissociation region

## 1 INTRODUCTION

Study of the physical and chemical properties of molecular clouds, their formation and evolution is crucial for understanding the star formation history and evolution of a galaxy such as our own, the Milky Way. The first critical step in this whole process is the formation of molecular clouds from diffuse atomic gas. A major hindrance in accessing this step lies in the fact that the molecular gas is primarily in the form of H<sub>2</sub> which has no allowed transitions that are excited in the cold environments of most of the interstellar material. Therefore, CO has long been used as a surrogate tracer of H<sub>2</sub> in the Milky Way (Bolatto et al. 2013; Miville-Deschênes et al. 2017). However, recent observational and theoretical studies suggest that CO is photodissociated to ionized and neutral C atom in a significant fraction of the diffuse molecular gas, with this phase termed as CO-dark molecular gas (Wolfire et al. 2010; Pineda et al. 2013, 2014). In the Milky Way, CO-dark H<sub>2</sub> gas is understood to comprise  $\sim 30$  per cent of the molecular mass (Pineda et al. 2013). Further, CO is known to get depleted onto dust grains in cold and dense environments (Whittet et al. 2010), and chemical fractionation may also influence the abundance of the <sup>12</sup>CO molecule relative to its isotopologues (Sheffer et al. 2007). Hence, observations of chemical species tracing diffuse interstellar clouds are vital in order to understand the transition from atomic to molecular phase. It is also necessary to identify alternative molecular tracers which are acces-

sible over a wide range of molecular hydrogen column densities and interstellar conditions.

As Liszt & Lucas (2002) pointed out, there are only a few species *viz.*, CH, OH, CN and CO, that can be observed in the optical/UV and radio domains, and hence provide an important bridge between two different ways of studying interstellar chemistry in diffuse clouds. Of these, CH was among the earliest molecular species to be detected in the diffuse ISM (Swings & Rosenfeld 1937; McKellar 1940; Adams 1941), and has been proven to have a very well-determined abundance relative to H<sub>2</sub>. It is found to be nearly constant for all lines of sight with  $A_{\text{V}} < 3$ , with a mean  $N(\text{CH})/N(\text{H}_2) = (4.3 \pm 1.9) \times 10^{-8}$ , and  $N(\text{CH}) \propto N(\text{H}_2)^{1.00 \pm 0.06}$  for  $10^{19} < N(\text{H}_2) < 10^{21}$  cm<sup>-2</sup> (Liszt & Lucas 2002). The tight correlation between the CH and H<sub>2</sub> abundances is understood based on the higher formation rates of CH in reactions involving molecular hydrogen. Based on a fit, Sheffer et al. (2008) constrained  $N(\text{CH})/N(\text{H}_2)$  to a value of  $3.5 \times 10^{-8}$ , which is consistent with the results for dark clouds with  $N(\text{H}_2) < 6 \times 10^{21}$  cm<sup>-2</sup> (Mattila 1986).

OH absorption in the Galaxy has also been studied since long, using observations at radio wavelengths (Weinreb et al. 1963), as well as through the ultraviolet electronic transitions (Crutcher & Watson 1976; Chaffee & Lutz 1977). Like CH, the OH molecule has also been explored as a surrogate for H<sub>2</sub>, particularly in diffuse molecular gas without CO, as the ground-state main lines of OH in the radio regime are readily detectable in translucent/diffuse molecular clouds (e.g., Magnani & Siskind 1990; Barriault et al. 2010). OH is considered to be a precursor molecule for the formation of CO in diffuse regions (Black & Dalgarno 1977; Barriault et al. 2010). Models of the diffuse ISM also indicate that OH absorbers with column

\* E-mail: katherine.rawlins@gmail.com

† E-mail: bhaswati@tifr.res.in

densities in the range  $10^{13} - 10^{14} \text{ cm}^{-2}$  trace CO-dark molecular gas (Balashev et al. 2021). However, in order to establish OH as a bona-fide tracer of  $\text{H}_2$ , the OH/ $\text{H}_2$  abundance ratio,  $X_{\text{OH}} = N_{\text{OH}}/N_{\text{H}_2}$ , must be constrained. This is a challenge due to the limited direct observations of  $\text{H}_2$  for sightlines where OH is detected. Based on near-UV observations of six sightlines, previous studies estimated the  $N(\text{OH})/N(\text{H}_2)$  ratio to be  $\sim 1.0 \times 10^{-7}$  (Liszt & Lucas 2002; Weselak et al. 2009, 2010). Additionally, a definite correlation between the OH and CH column densities in diffuse/translucent clouds has been deduced based on a larger sample of twenty-four sightlines, which in turn indicates an indirect correlation between OH and  $\text{H}_2$  (Mookerjee 2016; Weselak et al. 2009, 2010).

Astrochemical models have indicated values of  $X_{\text{OH}}$  ranging from  $10^{-7}$  (Black & Dalgarno 1977) and  $1.6 \times 10^{-8} - 2.9 \times 10^{-7}$  for  $A_V = 0.6 - 2.1$  mag (Van Dishoeck & Black 1986). Weselak et al. (2009) were unable to draw conclusions about any underlying correlation between observed column densities of OH and  $\text{H}_2$  on account of sparse UV data (only six observations). But recent radio observations have obtained a typical value of  $X_{\text{OH}} \sim 10^{-7}$  (Nguyen et al. 2018; Rugel et al. 2018; Tang et al. 2021). Observational studies detecting higher values of OH abundance of a few times  $10^{-7}$  in molecular boundaries, find the value to decrease towards  $X_{\text{OH}} = 10^{-7}$  at visual extinctions  $A_V \geq 2.5$  mag (Xu et al. 2016). Far-infrared absorption studies of the  ${}^2\Pi_{3/2}J = 5/2 \leftarrow 3/2$  transition of OH at 2514.3 GHz measure OH abundances between  $10^{-8} - 10^{-6}$  (Wiesemeyer et al. 2016; Jacob et al. 2022). However,  $N(\text{H}_2)$  used by these longer wavelength studies, are not direct measurements. Typically, molecular clouds capable of attenuating the UV radiation field imply that the OH abundance can no longer be constant. Depending on the radiation field at  $A_V \sim 6$  mag, oxygen-bearing species are depleted onto ice in the grain mantles, thus affecting the OH abundance (Hollenbach et al. 2012).

Some near-UV Galactic sightlines in the literature are reported to host  $\text{OH}^+$  along with OH. First observed in the interstellar medium only a few years ago at microwave (Wyrowski et al. 2010), UV (Krelowski et al. 2010) and far-infrared (Neufeld et al. 2010) wavelengths, several more near-ultraviolet detections of  $\text{OH}^+$  along Galactic sightlines have been made subsequently (Porras et al. 2014; Bacalla et al. 2019; Weselak 2020). Recently, Weselak (2020) found that the column densities of OH and  $\text{OH}^+$  are strongly correlated for the available sample of fourteen sightlines.

OH has been known to exist in a few intervening absorbers outside the Milky Way too (eg. Chengalur et al. 1999; Kanekar et al. 2003). Improved observational capabilities in the radio regime have brought about renewed interest in probing diffuse extragalactic gas for the presence of OH (Gupta et al. 2018, 2021). Thus, constraining the OH abundance,  $X_{\text{OH}}$ , in the Galaxy will also be useful for studies of molecular chemistry and abundances in other galaxies and high-redshift environments.

In this paper, we have performed a combined analysis of archival and literature data on near-ultraviolet absorption measurements of vibronic transitions of OH along twenty-three sightlines (ten of them new) for which measurements of  $N(\text{H}_2)$  are available. This data is combined with data available in literature to study the correlation between OH column densities and column densities of H I,  $\text{H}_2$ , CH and  $\text{OH}^+$ . Observed column densities and/or abundances are compared with the calculations of models for diffuse photodissociation regions in order to, (a) gain insight into the impact of density and radiation field on the abundances, and (b) understand the physical properties of the diffuse interstellar clouds hosting these molecules.

The spectroscopic data analysis and subsequent results are presented in Section 2 and Section 3 respectively. Details and results

of the numerical models are described in Section 4, followed by a discussion in Section 5 and a summary in Section 6.

## 2 NEAR-UV SPECTROSCOPY

### 2.1 Data & Basic Analysis Methods

In order to detect OH in diffuse interstellar clouds, we identified from literature, potential sightlines in the direction of bright Galactic sources in which, either (i) molecules such as CH and/or CN have been detected (Sheffer et al. 2008), and/or (ii) estimates of  $N(\text{H}_2)$  are available (Rachford et al. 2002, 2009; Shull et al. 2021). For these selected sightlines, we retrieved reduced high-resolution near-ultraviolet spectra from the science archive of the European Southern Observatory (<https://archive.eso.org/scienceportal/home>). All spectra had been obtained using the Ultraviolet and Visual Echelle Spectrograph at Very Large Telescope, Chile, at a resolution higher than 40,000.

Multiple spectra for a particular sightline were first co-added using PyRAF routines (Science Software Branch at STScI 2012). The resultant spectrum was then normalized locally for regions around the absorption lines of interest by performing a linear fit. The observed spectrum was then divided by the fitted continuum, and selected transitions of OH, CH and  $\text{OH}^+$  (Table 1) were identified in the normalized spectrum.

The equivalent widths of the absorption features were determined as follows:

$$W = \Delta\lambda \sum_{n=1}^M \left(1 - \frac{F}{F_c}\right) \quad (1)$$

where  $\Delta\lambda$  is the spectral dispersion,  $M$  is the number of pixels associated with the absorption line,  $F$  and  $F_c$  refer to the actual flux and the continuum level respectively for a particular pixel.

The column density values were calculated under the optically thin approximation using:

$$N = 1.13 \times 10^{20} \frac{W}{\lambda_r^2 f_{\text{osc}}} \quad (2)$$

where  $N$  is the column density,  $\lambda_r$  is the rest wavelength of the transition and  $f_{\text{osc}}$  is the oscillator strength. Table 1 presents the rest wavelengths and oscillator strengths of the probed transitions. The uncertainty in equivalent width is estimated using the relation:

$$\sigma^2(W) = \frac{h_\lambda}{S/N} \sum_{j=1}^M \left(\frac{F_j}{F_c}\right)^2 + \left[\frac{\sigma(F_c)}{F_c}(\delta\lambda - W)\right]^2 \quad (3)$$

where  $h_\lambda$  is the spectral dispersion per pixel,  $F_j$  is the flux in the  $j$ th pixel, and  $\delta\lambda$  is the extent of the absorption line (Chalabaev & Maillard 1983, Appendix). The signal-to-noise ratio,  $S/N$ , is related to the flux, as follows:

$$\sigma(F_j) = \frac{F_j}{S/N} \quad (4)$$

The column density,  $N$ , has an uncertainty which is estimated in the following manner:

$$\sigma(N) = \sigma(W) \times N/W \quad (5)$$

The total column density of OH is determined by adding the column densities derived from the equivalent widths of the 3078 and 3082 Å transitions. Similarly, the total CH column density is the sum of the individual column densities obtained from the 3137 and 3143 Å transitions.

**Table 1.** Transitions probed for each diffuse Galactic sightline

Species	Vibronic band	Rotational line	Wavelength (Å)	Oscillator strength	Reference
OH	A <sup>2</sup> Σ <sup>+</sup> -X <sup>2</sup> Π <sub>i</sub> (0,0)	Q <sub>1</sub> (3/2)+ <sup>o</sup> P <sub>21</sub> (3/2)	3078.443	0.00105	Weselak et al. (2009)
		P <sub>1</sub> (3/2)	3081.6643	0.000648	Weselak et al. (2009)
CH	C <sup>2</sup> Σ <sup>+</sup> -X <sup>2</sup> Π <sub>i</sub> (0,0)	R <sub>2</sub>	3137.576	0.00210	Lien (1984)
		Q <sub>2</sub> (1)+ <sup>o</sup> R <sub>12</sub> (1)	3143.150	0.00640	Lien (1984)
OH <sup>+</sup>	A <sup>3</sup> Π-X <sup>3</sup> Σ <sup>-</sup> (0,0)	<sup>r</sup> R <sub>11</sub> (0)	3583.757	0.000527	Hodges et al. (2018)

## 2.2 Sample of OH sightlines

Spectra for thirty diffuse Galactic lines-of-sight were extracted from the archival data and analysed. Along ten of these sightlines, OH was detected and seven among them lie within  $\sim 10$  degrees of the Galactic disk. While the sightline towards HD23180 was previously observed (Chaffee & Lutz 1977; Weselak et al. 2009), we independently analysed the spectrum following the methods used for the remaining nine new sightlines. It is this updated value that we consider in our further analysis and discussion.

Table A1 presents details of the OH sightlines. Even though several more diffuse absorbers were identified and analysed based on known CH, CN or H<sub>2</sub> absorption, these are not included as part of the new results presented henceforth in this paper.

Table 2 presents the measured equivalent widths of the OH absorption lines at 3078 and 3082 Å, along with the column densities of OH and CH for the ten OH sightlines. H<sub>2</sub> column densities for these absorbers reported in literature are also tabulated (Savage et al. 1977; Rachford et al. 2002; Cartledge et al. 2004; Rachford et al. 2009; Dirks & Meyer 2019; Shull et al. 2021). For four of the new sightlines, we have also determined the OH<sup>+</sup> column densities based on the  $\lambda$ 3583 absorption feature, and using the improved oscillator strength of Hodges et al. (2018). Two of these are new detections – the sightlines towards HD62542 and HD168076. OH<sup>+</sup> has been previously detected in the other two absorbers, that is, along the line-of-sight to HD41117 and HD179406 (Krełowski et al. 2010; Bacalla et al. 2019; Weselak 2020), and the column densities we estimate are consistent with the values in literature. The column densities for which S/N < 3, are marked with upper limits in Table 2, and are not treated in any of the numerical estimates hereafter.

Throughout the paper, "This work" refers to the positive OH detections from the current analysis. Additionally, there are thirteen sightlines in literature for which column densities of OH, CH and H<sub>2</sub> are available, (twelve of these with  $N(\text{OH}) > 3\sigma$ ), and a further eleven sightlines for which column densities of OH and CH are available but with no corresponding  $N(\text{H}_2)$  measurements (nine of these with  $N(\text{OH}) > 3\sigma$ ). The OH and CH column densities taken from literature are from Weselak et al. (2009, 2010); Bhatt & Cami (2015); Mookerjee (2016), with further details of the specific sightlines provided in the footnotes of Table 2. Thus, by combining the sightlines from literature with those we have newly analyzed, the total sample size with S/N > 3σ is twenty-six (Table 2). OH<sup>+</sup> is also detected in twelve of the twenty-three primary sightlines for which  $N(\text{H}_2)$  is available (three of these with  $N(\text{OH}^+) > 3\sigma$ ). The measured  $E(B-V)$  values towards the OH sightlines range between 0.28 to 1.59 mag, corresponding to a range of 0.9 to 4.9 mag of visual extinction  $A_V$  (for an  $R_V$  of 3.1).

## 3 CORRELATIONS BETWEEN OBSERVED QUANTITIES

We first explore the correlations between the OH, CH, H<sub>2</sub> and H<sub>tot</sub> column densities and  $E(B-V)$  pair-wise (Fig. 1), by calculating the Pearson correlation coefficient. The standard error in the correlation coefficient is estimated using  $\sigma_r = (1-r^2)/\sqrt{n-1}$ , as done by Weselak (2020). Here,  $r$  is the Pearson correlation coefficient and  $n$  is the number of data points. While deriving the correlations, wherever possible, we have included data from literature, e.g., data from Sheffer et al. (2008) for the  $N(\text{CH})-N(\text{H}_2)$  relation.

Table 3 presents the correlation coefficients between pairs of column densities and extinction properties, along with the critical values of the Pearson  $r$  coefficient that correspond to a 5% possibility that the correlation factor arises by chance. We find the correlation coefficients for several pairs of quantities to be larger than the critical values (Table 3).

### 3.1 CH, OH and H<sub>tot</sub> correlations with $E(B-V)$

The twenty-three sightlines with H<sub>2</sub> column density measurements show  $N(\text{H}_2)$  between  $(0.8-14.45) \times 10^{20} \text{ cm}^{-2}$ , and  $N(\text{H I})$  between  $(4.27-58.88) \times 10^{20} \text{ cm}^{-2}$ . Most of the sightlines are predominantly atomic, with only four (toward HD73882, HD152236, HD154368 and HD210121) sightlines having molecular hydrogen fraction exceeding 50%. The total hydrogen column density,  $N(\text{H}_{\text{tot}}) = N(\text{H I}) + 2 N(\text{H}_2)$ , is strongly correlated with  $E(B-V)$  with a Pearson  $r = 0.73$ , and the fitted relation between the total hydrogen nuclei column density and  $E(B-V)$  is  $N(\text{H}_{\text{tot}}) = (7.27 \pm 0.46) \times 10^{21} \text{ cm}^{-2} E(B-V)$ . Bohlin et al. (1978) had famously obtained the frequently quoted constant of proportionality,  $N(\text{H}_{\text{tot}}) = 5.8 \times 10^{21} E(B-V)$  for lines-of-sight with  $E(B-V)$  values not exceeding 0.4 mag. In a more recent work, Liszt (2014) has obtained the relation  $N(\text{H I}) = 8.3 \times 10^{21} \text{ cm}^{-2} E(B-V)$  for primarily atomic lines of sight with  $E(B-V) < 0.1$  mag. The lines of sight analysed here, though primarily atomic, have significantly larger  $E(B-V)$  values, which have mostly been measured using UV extinction (Rachford et al. 2009; Shull et al. 2021). The  $N(\text{CH})-E(B-V)$  scatterplot shows a definite correlation between the two quantities and a negative intercept on the y-axis which is consistent with the results towards dark clouds (Liszt & Lucas 2002, and references therein). We obtain a relation of  $N(\text{CH}) = (6.66 \pm 0.72) \times 10^{13} \times E(B-V)$  when fitted with a straight line without an intercept. This compares well within uncertainties with  $N(\text{CH}) = 0.5 \times 3 \times 10^{-8} \times 5.8 \times 10^{21} E(B-V) \text{ cm}^{-2} = 8.7 \times 10^{13} E(B-V) \text{ cm}^{-2}$  which is an estimate of the maximum CH column density for  $X_{\text{CH}} = 3 \times 10^{-8}$  if all gas along the line-of-sight were in the form of H<sub>2</sub>. OH also has significant moderate correlation with  $E(B-V)$ , with a Pearson coefficient of  $0.55 \pm 0.14$ .

**Table 2.** OH equivalent widths and column densities of various molecular species for the Galactic sightlines with OH detection

Source	$E(B-V)$	$EW(3078)$ (mÅ)	$EW(3082)$ (mÅ)	$N(\text{OH})$ ( $10^{13} \text{ cm}^{-2}$ )	$N(\text{H}_2)$ ( $10^{20} \text{ cm}^{-2}$ )	Ref.	$N(\text{H I})$ ( $10^{20} \text{ cm}^{-2}$ )	Ref.	$N(\text{CH})$ ( $10^{13} \text{ cm}^{-2}$ )	$N(\text{OH}^+)$ ( $10^{13} \text{ cm}^{-2}$ )	Ref.
<b>This work</b>											
HD23180	0.29	$1.14 \pm 0.40$	$1.00 \pm 0.23$	$< 3.09$	$4.07 \pm 0.61$	1	$7.08 \pm 0.64$	11	$0.83 \pm 0.04$	...	...
HD41117	0.45	$2.60 \pm 1.38$	$1.62 \pm 0.81$	$< 5.89$	$4.90 \pm 0.49$	2	$25.12 \pm 3.77$	2	$0.83 \pm 0.07$	$5.78 \pm 1.01$	...
HD46202	0.49	$5.40 \pm 2.62$	$4.52 \pm 2.77$	$14.38 \pm 2.01$	$4.79 \pm 0.29$	2	$38.02 \pm 5.70$	11	$1.07 \pm 0.10$	...	...
HD62542	0.35	$6.69 \pm 1.19$	$4.43 \pm 0.84$	$15.80 \pm 2.06$	$6.46 \pm 1.36$	3	$8.51 \pm 2.55$	3	$3.31 \pm 0.56$	$< 2.56$	...
HD73882	0.69	$4.35 \pm 0.89$	$3.15 \pm 0.63$	$10.70 \pm 3.54$	$13.49 \pm 1.03$	3	$12.88 \pm 1.93$	2, 12	$3.16 \pm 0.22$	...	...
HD147683	0.39	$4.80 \pm 1.17$	$2.97 \pm 1.97$	$< 11.00$	$3.80 \pm 0.53$	4	5.25	13	$3.55 \pm 1.03$	...	...
HD147888	0.51	$2.54 \pm 0.96$	$2.14 \pm 0.77$	$< 6.76$	$2.95 \pm 0.15$	2	$27.54 \pm 8.26$	2	$2.63 \pm 0.37$	...	...
HD168076	0.78	$5.82 \pm 1.14$	$2.51 \pm 0.47$	$11.22 \pm 1.56$	$4.79 \pm 0.38$	3	$44.67 \pm 10.27$	11	$2.64 \pm 0.32$	$2.29 \pm 0.72$	...
HD179406	0.33	$3.12 \pm 0.99$	$1.25 \pm 0.78$	$< 5.89$	$5.37 \pm 0.38$	2	$16.98 \pm 5.09$	2, 14	$2.14 \pm 0.28$	$< 2.59$	...
HD203532	0.28	$5.07 \pm 0.91$	$4.80 \pm 1.09$	$14.57 \pm 2.25$	$4.37 \pm 0.39$	5	$18.62 \pm 1.68$	5	$3.24 \pm 0.65$	...	...
<b>OH and CH sightlines from literature<sup>a,b</sup>: H<sub>2</sub> available</b>											
HD24398	0.29	$1.67 \pm 0.08$	$1.11 \pm 0.05$	$3.93 \pm 0.18$	$4.68 \pm 0.47$	6, 7	$6.46 \pm 0.52$	11	$2.84 \pm 0.29$	$< 0.50$	19
HD27778	0.38	$5.30 \pm 0.15$	$2.20 \pm 0.10$	$10.10 \pm 0.40$	$6.17 \pm 0.37$	3	$9.55 \pm 2.86$	3	$3.37 \pm 0.77$	...	...
HD34078	0.49	$1.72 \pm 0.27$	$0.86 \pm 0.21$	$3.53 \pm 0.69$	$6.46 \pm 0.19$	7, 8	$15.85 \pm 1.74$	11	$7.34 \pm 0.99$	...	...
HD110432	0.40	$1.81 \pm 0.41$	$1.28 \pm 0.34$	$4.41 \pm 1.09$	$4.37 \pm 0.18$	3	$7.08 \pm 1.06$	15	$1.92 \pm 0.22$	$< 0.67$	20, 21
HD147933	0.46	$3.63 \pm 0.27$	$2.02 \pm 0.31$	$7.83 \pm 0.88$	$3.73 \pm 1.07$	1	$43.65 \pm 3.93$	11	$2.73 \pm 0.17$	...	...
HD149757	0.32	$2.01 \pm 0.67$	$1.25 \pm 0.32$	$4.58 \pm 1.35$	$4.49 \pm 0.64$	1	$4.90 \pm 0.49$	11	$3.10 \pm 0.19$	...	...
HD151932	0.60	$4.46 \pm 0.71$	$2.13 \pm 0.54$	$8.97 \pm 1.80$	$5.89 \pm 0.59$	9	$24.55 \pm 2.70$	11	$2.72 \pm 0.15$	$< 1.82$	20, 21
HD152236	0.66	$3.50 \pm 0.44$	$2.41 \pm 0.34$	$8.40 \pm 1.12$	$5.37 \pm 0.64$	2	$58.88 \pm 8.83$	2, 11	$2.72 \pm 0.30$	$< 2.00$	20, 21
HD152249	0.42	$2.81 \pm 1.00$	$1.82 \pm 0.80$	$< 6.53$	$1.81 \pm 0.12$	10	$25.70 \pm 3.08$	11	$1.72 \pm 0.26$	$1.42 \pm 0.46$	20, 21
HD152270	0.50	$1.95 \pm 0.64$	$2.13 \pm 0.70$	$6.12 \pm 2.01$	$2.79 \pm 0.16$	10	$27.54 \pm 2.75$	10	$1.78 \pm 0.26$	...	...
HD154368	0.80	$9.25 \pm 0.58$	$4.01 \pm 0.31$	$17.90 \pm 1.20$	$14.45 \pm 3.74$	3	$10.00 \pm 0.50$	3, 16	$5.78 \pm 0.19$	$< 2.00$	20, 21
HD170740	0.48	$1.97 \pm 0.43$	$1.73 \pm 0.31$	$5.41 \pm 1.06$	$7.24 \pm 0.58$	3	$14.13 \pm 2.12$	11	$2.35 \pm 0.13$	$< 1.33$	20, 21
HD210121	0.38	$4.45 \pm 0.28$	$3.03 \pm 0.23$	$10.60 \pm 0.70$	$5.62 \pm 0.68$	3	$4.27 \pm 0.64$	3, 17	$3.29 \pm 0.17$	$< 1.33$	20, 21
<b>OH and CH sightlines from literature<sup>a,b</sup>: H<sub>2</sub> not available</b>											
BD-145037	1.59	$5.74 \pm 0.43$	$5.71 \pm 0.60$	$17.00 \pm 1.60$	...	...	...	...	$3.65 \pm 0.17$	2.48	19
HD114213	1.06	$9.86 \pm 0.96$	$8.30 \pm 0.87$	$26.40 \pm 2.70$	...	...	...	...	$4.35 \pm 0.22$	...	...
HD147889	1.02	$12.19 \pm 0.45$	$5.38 \pm 0.20$	$23.70 \pm 0.90$	...	...	50.12	12	$9.92 \pm 0.17$	...	...
HD148688	0.55	$0.92 \pm 0.45$	$0.81 \pm 0.54$	$< 2.53$	...	...	...	...	$1.61 \pm 0.17$	...	...
HD154445	0.37	$2.01 \pm 0.31$	$1.52 \pm 0.33$	$5.07 \pm 0.96$	...	...	$10.00 \pm 1.00$	11	$2.49 \pm 0.33$	$< 0.83$	20, 21
HD154811	0.66	$2.43 \pm 0.70$	$1.64 \pm 0.50$	$5.77 \pm 1.71$	...	...	...	...	$2.29 \pm 0.28$	...	...
HD161056	0.62	$10.71 \pm 0.61$	$6.78 \pm 0.50$	$24.60 \pm 1.60$	...	...	$16.98 \pm 3.40$	11	$5.62 \pm 0.24$	$< 3.00$	20, 21
HD163800	0.57	$2.00 \pm 0.17$	$1.85 \pm 0.12$	$5.67 \pm 0.41$	...	...	...	...	$3.29 \pm 0.10$	$< 2.00$	20, 21
HD164794	0.36	$1.55 \pm 0.40$	$1.00 \pm 0.65$	$< 3.59$	...	...	$19.50 \pm 1.36$	11	$1.19 \pm 0.25$	...	...
HD169454	1.10	$6.24 \pm 0.25$	$2.90 \pm 0.22$	$12.40 \pm 0.70$	...	...	...	...	$4.44 \pm 0.20$	...	...
HD172028	0.78	$5.05 \pm 0.50$	$4.09 \pm 0.35$	$13.20 \pm 1.20$	...	...	$17.30 \pm 0.80$	18	$5.96 \pm 0.24$	...	...

1 - Savage et al. (1977), 2 - Rachford et al. (2009), 3 - Rachford et al. (2002), 4 - Dirks & Meyer (2019), 5 - Cartledge et al. (2004), 6 - Wannier et al. (1999), 7 - Wolfire et al. (2008), 8 - Boissé et al. (2005), 9 - Rice (2018), 10 - Marggraf et al. (2004), 11 - Diplas & Savage (1994), 12 - Fitzpatrick & Massa (1990), 13 - Velusamy et al. (2017), 14 - Hanson et al. (1992), 15 - Rachford et al. (2001), 16 - Snow et al. (1996), 17 - Welty & Fowler (1992), 18 - Ádámkóvics et al. (2005), 19 - Bacalla et al. (2019), 20 - Krelowski et al. (2010), 21 - Weselak (2020)

<sup>a</sup> OH equivalent widths and column densities for the HD147889, HD154368, HD163800 and HD169454 sightlines are based on Bhatt & Cami (2015). For the remaining sightlines, the values are adopted from Weselak et al. (2009, 2010).

<sup>b</sup> CH column densities for the HD152236, HD152249, HD152270, HD154811 and HD164794 sightlines were obtained using the 3886 and 3890 Å transitions (Weselak et al. 2009, 2010). All other CH column density values from literature were determined through the 3137 and 3143 Å transitions. Of these, column densities for HD24398, HD27778, HD34078, HD110432, HD148688 and HD154445 are based on Mookerjea (2016), while the rest are from Bhatt & Cami (2015).

### 3.2 OH and CH correlations with H<sub>2</sub>

Based on the analysis of a compilation of  $N(\text{CH})$  and  $N(\text{H}_2)$  data, Liszt & Lucas (2002) had derived  $N(\text{CH}) = (4.3 \pm 1.9) \times 10^{-8} N(\text{H}_2)$  for  $10^{20} < N(\text{H}_2) < 2 \times 10^{21} \text{ cm}^{-2}$ . These column densities were collated from the results of UV and optical stellar absorption studies available at the time. Further, Sheffer et al. (2008) obtained a value of  $N(\text{CH}) = 3.5 \times 10^{-8} N(\text{H}_2)$ , also based on ultraviolet spectra. More recently, Weselak (2019) reported  $N(\text{H}_2)/N(\text{CH}) =$

$(2.01 \pm 0.09) \times 10^7$  with a negative intercept on the y-axis. This yields  $N(\text{CH}) = (4.98 \pm 0.22) \times 10^{-8} N(\text{H}_2)$ . Using an orthogonal distance regression suitable for the analysis of data with uncertainty in both x- and y-axes, we obtain an equivalent relation with a factor of  $(3.83 \pm 0.23) \times 10^{-8}$ , which is consistent with the result of Sheffer et al. (2008) and Liszt & Lucas (2002) within the limits of uncertainties.

Estimates of the OH column densities based on the measurements of the hyperfine transitions of the  $^2\Pi_{3/2}J = 3/2$  ground state of

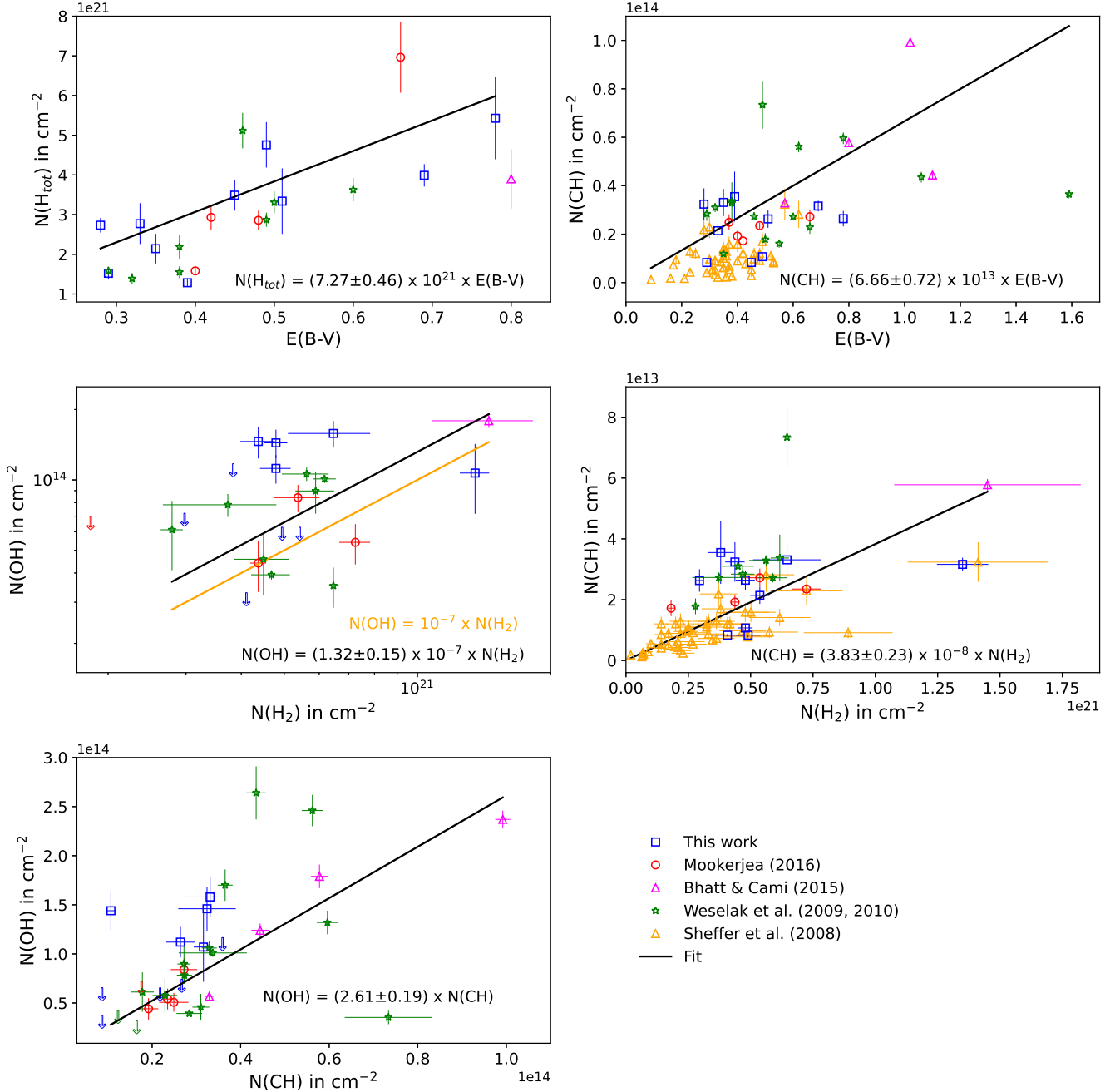


**Figure 1.** Correlations between molecular column densities and  $E(B-V)$  along OH and CH lines-of-sight studied in this work and in literature (refer to the common key for all plots). Observational data points in all plots are labelled according to the study which reports OH, except for Sheffer et al. (2008), from which only CH column densities are considered. Additional sightlines from literature have been included for certain correlation plots, as mentioned in the individual panels. The black straight line corresponds to the fit derived by using the method of orthogonal distance regression, which accounts for uncertainties in quantities plotted along both abscissa and ordinate. The equation of the fit is mentioned in the corresponding panel. Table 3 presents the calculated Pearson  $r$  correlation coefficients.

OH in the 18-cm band (Rugel et al. 2018; Tang et al. 2021), as well as using the group of hyperfine transitions  ${}^2\Pi_{3/2}J = 5/2 \leftarrow 3/2$  at 2514.3 GHz (Wiesemeyer et al. 2012, 2016) are available in the literature. The  $N(\text{H}_2)$  values for the OH sightlines in these studies are not direct measurements, but are scaled estimates obtained from  $N(\text{CH})$  or  $N(\text{HF})$  (Wiesemeyer et al. 2012, 2016),  ${}^{13}\text{CO}$  (Rugel et al. 2018), or  $E(B-V)$  (Tang et al. 2021). Thus, we do not include the far-infrared and radio measurements in our analysis of the OH-H<sub>2</sub> re-

lation. Analysing the seventeen UV sightlines in our study with OH and H<sub>2</sub>, we determine a correlation coefficient of  $0.44 \pm 0.20$ , which is less than the critical value of 0.48 for the Pearson  $r$  when  $p = 0.05$ . Applying orthogonal distance regression, we obtain  $N(\text{OH})/N(\text{H}_2) = (1.32 \pm 0.15) \times 10^{-7}$ , while the median value obtained for the same ratio is  $1.56 \times 10^{-7}$ . Both these values are significantly higher than the previous estimate of  $\sim 1.0 \times 10^{-7}$  (Liszt & Lucas 2002; Weselak et al. 2009, 2010).

**Table 3.** Pearson correlation coefficients between the OH, CH, H<sub>2</sub> and H<sub>tot</sub> column densities and  $E(B-V)$ . Correlations are based on data from the present analysis and from literature (Weselak et al. 2009, 2010; Bhatt & Cami 2015; Mookerjea 2016). Additional data, where included, are mentioned below the table. The critical value corresponds to the  $r$ -value which confirms existence of correlation with 95% confidence.

Relation	Pearson coefficient $r$	$n^\dagger$	Critical $r$ for $p = 0.05$
$N(\text{CH})$ vs $N(\text{H}_2)$	$0.66 \pm 0.07$	$73^a$	0.23
$N(\text{OH})$ vs $N(\text{CH})$	$0.51 \pm 0.15$	$26^b$	0.39
$N(\text{OH})$ vs $N(\text{H}_2)$	$0.44 \pm 0.20$	$17^b$	0.48
$N(\text{H}_2)$ vs $E(B-V)$	$0.55 \pm 0.15$	23	0.41
$N(\text{H}_{\text{tot}})$ vs $E(B-V)$	$0.73 \pm 0.10$	23	0.41
$N(\text{CH})$ vs $E(B-V)$	$0.59 \pm 0.05$	$84^a$	0.22
$N(\text{OH})$ vs $E(B-V)$	$0.55 \pm 0.14$	$26^b$	0.39

<sup>†</sup>  $n$ : Number of data points

<sup>a</sup> Includes data from Sheffer et al. (2008).

<sup>b</sup> Only  $N(\text{OH})$  measurements with  $S/N > 3\text{-}\sigma$  are included.

The scatter plot between  $N(\text{OH})$  and  $N(\text{CH})$  shows reasonably good correlation, with the exception of three sightlines – HD34078, HD114213 and HD161056, with  $E(B-V) = 0.49, 1.06$  and  $0.62$  respectively. The first of these sightlines has very low OH column density, while the other two show significantly higher values of  $N(\text{OH})$  (Fig 1). The median of the observed values of  $N(\text{OH})/N(\text{CH})$  is 3.04, and the fitted value of  $N(\text{OH})/N(\text{CH})$  is  $2.61 \pm 0.19$ . These estimates are consistent with results in literature (Liszt & Lucas 2002; Weselak et al. 2010; Mookerjea 2016). The  $N(\text{OH})/N(\text{CH})$  ratio for individual sightlines in our sample ranges from 0.4 to 13.5, with only two out of the twenty-six lines-of-sight having values outside the range 1–5 (sightlines with  $S/N > 3$  only).

#### 4 NUMERICAL MODELS OF THE DIFFUSE INTERSTELLAR CLOUDS

OH<sup>+</sup>, the precursor to the formation of OH, can be produced through two different channels (Draine 2011; Gerin et al. 2016). One route is through the fast exothermic reaction between O and H<sub>3</sub><sup>+</sup>:  $\text{O} + \text{H}_3^+ \rightarrow \text{OH}^+ + \text{H}_2$ . The H<sub>3</sub><sup>+</sup> necessary for this reaction is generated by cosmic ray ionization of H<sub>2</sub>, that is,  $\text{H}_2 + \text{CR} \rightarrow \text{H}_2^+ + \text{e}^-$ , followed rapidly by  $\text{H}_2^+ + \text{H}_2 \rightarrow \text{H}_3^+ + \text{H}$ . The second channel for OH<sup>+</sup> formation occurs through charge exchange between oxygen and hydrogen:  $\text{O} + \text{H}^+ \rightarrow \text{O}^+ + \text{H}$ , followed by  $\text{O}^+ + \text{H}_2 \rightarrow \text{OH}^+ + \text{H}$  (Liszt 2003). Once OH<sup>+</sup> is available, the reaction  $\text{OH}^+ + \text{H}_2 \rightarrow \text{H}_2\text{O}^+ + \text{H}$  occurs, forming a water ion and a hydrogen atom. The newly created H<sub>2</sub>O<sup>+</sup>, in 20% of the cases, forms OH and H in a dissociative recombination reaction with a free electron:  $\text{H}_2\text{O}^+ + \text{e}^- \rightarrow \text{OH} + \text{H}$ . The principal way in which OH is produced in diffuse and translucent clouds, is similar to the previous reaction sequence in that it involves dissociative recombination and starts with H<sub>2</sub>O<sup>+</sup>, but takes a few more steps to form OH (Singh & de Almeida 1980):  $\text{H}_2\text{O}^+ + \text{H}_2 \rightarrow \text{H}_3\text{O}^+ + \text{H}$ ;  $\text{H}_3\text{O}^+ + \text{e}^- \rightarrow \text{OH} + \text{H}_2$  (14%) or  $\text{H}_3\text{O}^+ + \text{e}^- \rightarrow \text{OH} + \text{H} + \text{H}$  (60%). The OH thus formed, is primarily destroyed by photodissociation:  $\text{OH} + \text{h}\nu \rightarrow \text{O} + \text{H}$ .

#### 4.1 Modelling technique

In order to constrain the physical environment of the diffuse Galactic clouds associated with the observed OH and CH absorption features, we set up a grid of numerical models using the spectral synthesis code CLOUDY, version c17.02 (Ferland et al. 2017). Each model assumes a diffuse cloud of uniform density with the plane-parallel geometry of a photodissociation region (Tielens & Hollenbach 1985), and illuminated from both sides by an ISRF ( $\chi$ ), with intensities expressed in units of the Habing FUV radiation field,  $G_0$  (Habing 1968). We consider solar metallicity and cosmic ray ionization rate of  $2 \times 10^{-16} \text{ s}^{-1}$ , estimated as the mean Galactic value by Indriolo et al. (2007). Graphite and silicate dust grains are included in the model calculations, as per the size distribution proposed by Mathis et al. (1977). Metal depletion on grain surface is also considered in accordance with the overall elemental and grain abundances. We have run a grid of models with different sets of values of total density of hydrogen nuclei,  $n_{\text{H}}$ , and intensity of the ISRF,  $\chi$ . For each set of parameter values, we model six clouds with different H<sub>2</sub> column densities that span the entire range of  $N(\text{H}_2)$  seen in our OH sightline sample. The extent of the modelled absorbers thus, depends on the corresponding H<sub>2</sub> column density. The CLOUDY calculations stop at these specified values of  $N(\text{H}_2)$  (Table A2), and the corresponding column densities for all other chemical species are then noted down and used for comparison with the observational data. Table A2 presents all parameter values considered for the diffuse cloud models.

#### 4.2 Physical conditions in the diffuse clouds

The temperature in the coolest, molecular part of these modelled clouds lies in the range 16 to 30 K for the models corresponding to the largest column densities of H<sub>2</sub>. The extent of the absorbers is less than or up to a few parsecs, and the value of  $A_V$  in these models is within  $\sim 2$  mag. These values are consistent with the expectations for diffuse/translucent clouds (Snow & McCall 2006).

We have compared the observed scatterplots of  $N(\text{OH})$ ,  $N(\text{CH})$ ,  $N(\text{OH})/N(\text{CH})$ ,  $X_{\text{OH}}$  and  $X_{\text{CH}}$  as functions of  $N(\text{H}_2)$  with the corresponding predictions from the diffuse cloud models explored using CLOUDY (Fig. 2). The grid of models span the range of  $N(\text{H}_2)$  covered by the OH and CH data presented here and in literature (Weselak et al. 2009, 2010; Bhatt & Cami 2015; Mookerjea 2016). Additional data points from observations available in literature have also been included if they lie in the aforementioned range of  $N(\text{H}_2)$ .

The observed  $N(\text{OH})-N(\text{H}_2)$  correlation can be reproduced by diffuse cloud models with number density  $50 \text{ cm}^{-3}$  and FUV radiation field intensity,  $\chi$ , ranging between 0.5 to 5  $G_0$ , with the predicted value of  $N(\text{OH})$  for the same value of  $N(\text{H}_2)$  increasing as the radiation field intensity increases (Fig. 2). Although we find that the  $n_{\text{H}} = 100 \text{ cm}^{-3}$  models with  $\chi = 1 G_0$  predict lower values of  $N(\text{OH})$ , these models could, in principle, reproduce the observed higher values of  $N(\text{OH})$  for larger values of ISRF intensity. The models with  $n_{\text{H}} = 500 \text{ cm}^{-3}$  however produce significantly lower values of  $N(\text{OH})$ , and hence, are not plotted. Thus, based on the model predictions, OH absorption appears to arise primarily from extremely diffuse ( $n_{\text{H}} \sim 50 \text{ cm}^{-3}$ ) interstellar clouds.

In the plot of OH abundance ( $X_{\text{OH}}$ ) relative to H<sub>2</sub>, we have also shown a horizontal line corresponding to the value of  $X_{\text{OH}} = 10^{-7}$  that is widely used in literature. We find that the  $X_{\text{OH}}$  values estimated from this work and literature (Weselak et al. 2009, 2010; Bhatt & Cami 2015; Mookerjea 2016), lie in the range  $0.5-5 \times 10^{-7}$ , on both sides of this nominal value of  $10^{-7}$ . Al-

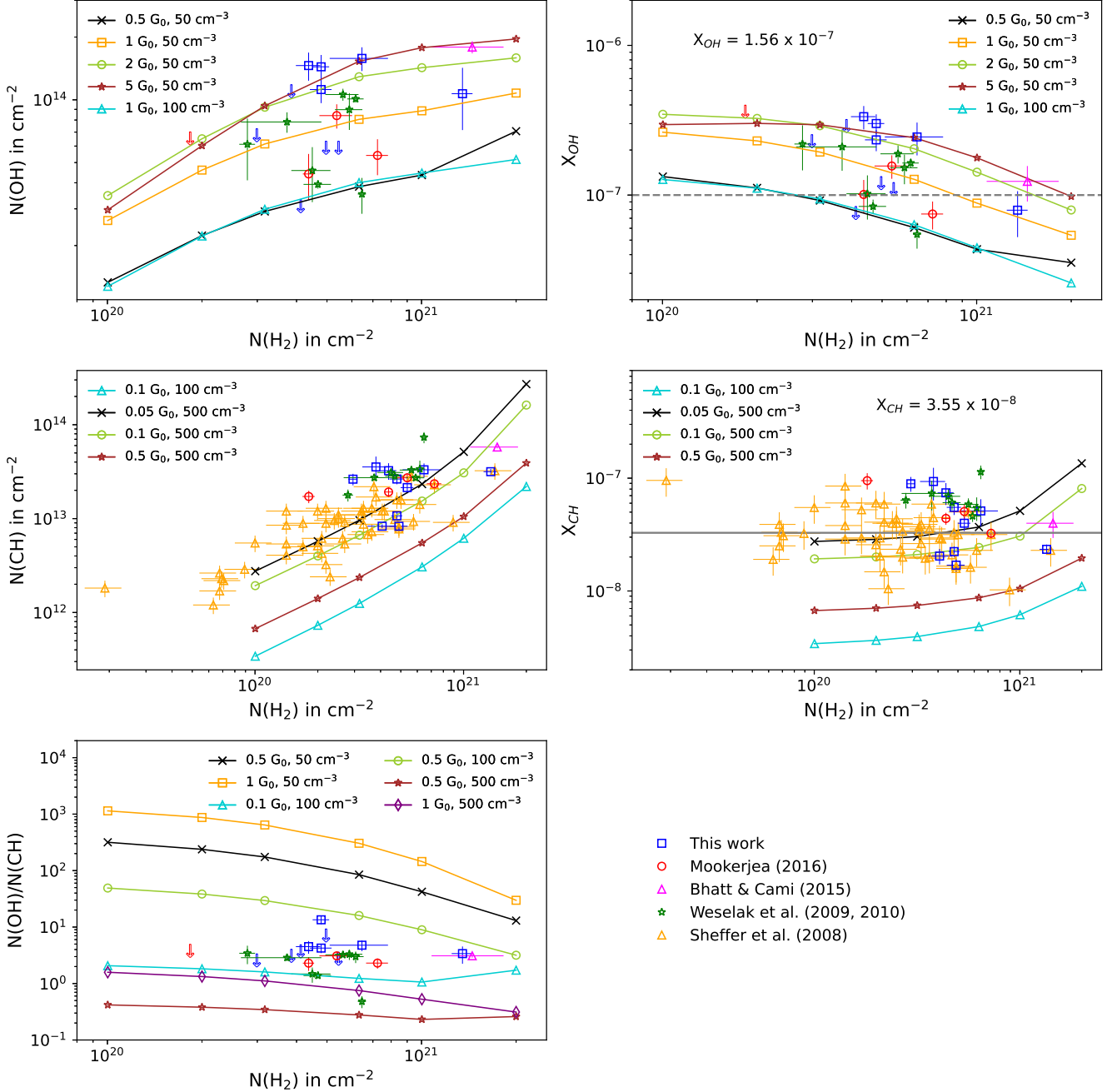


**Figure 2.** Comparison of the observed column density and abundance relations of OH and CH with the corresponding predictions from CLOUDY models. Physical properties of these diffuse Galactic clouds, that is, the intensity of radiation field and hydrogen density, can be constrained from these plots. All models assume solar metallicity and the Galactic background cosmic ray ionization rate of  $2 \times 10^{-16} \text{ s}^{-1}$  (Indriolo et al. 2007). The  $X_{\text{OH}}$  and  $X_{\text{CH}}$  values mentioned in the panels are median values. OH and CH observations are from this work and literature (refer to the common key for all plots). Observational data points in all plots are labelled according to the study which reports OH, except for Sheffer et al. (2008), from which only CH column densities are considered.

though not included in the comparison with the CLOUDY models constructed by us, the radio measurements of the 18-cm OH band by Rugel et al. (2018) and the far-infrared measurements of Wiesemeyer et al. (2012, 2016) also agree with this range of  $X_{\text{OH}}$ . But the values from Tang et al. (2021) consistently show values well in excess of  $10^{-7}$ , going up to  $4 \times 10^{-6}$ . However, these FIR and radio estimates of  $X_{\text{OH}}$  are not based on direct H<sub>2</sub> measurements,

and are therefore, not combined with the values obtained from our near-UV analysis.

The lower density models which are consistent with the  $X_{\text{OH}}$  values observed in the near-UV (This work and Weselak et al. 2009, 2010; Mookerjee 2016) show an almost constant  $X_{\text{OH}}$  with increasing  $N(\text{H}_2)$  up to a column density  $\sim 7 \times 10^{20} \text{ cm}^{-2}$ . This is followed by a decreasing trend at still larger values of  $N(\text{H}_2)$ . The models with  $n_{\text{H}} = 500 \text{ cm}^{-3}$  however, predict  $X_{\text{OH}}$  significantly lower than

the observed values. The value of  $X_{\text{OH}}$  predicted by the model with  $n_{\text{H}} = 50 \text{ cm}^{-3}$  and  $\chi = 0.5 G_0$  is similar to the value predicted by the model with  $n_{\text{H}} = 100 \text{ cm}^{-3}$  and  $\chi = 1 G_0$ , thus indicating that  $X_{\text{OH}}$  depends on  $\chi/n_{\text{H}}$ .

In case of the  $N(\text{CH})$ – $N(\text{H}_2)$  relation, the models predict values consistent with observations only for high density and low ISRF intensity, that is, for models with  $n_{\text{H}} = 500 \text{ cm}^{-3}$  and  $\chi$  between 0.05 and  $0.1 G_0$ . Further,  $N(\text{CH})$  is seen to increase with decreasing values of radiation field intensity. For models with  $\chi = 0.5 G_0$  and  $n_{\text{H}} = 100 \text{ cm}^{-3}$ , the values of predicted  $N(\text{CH})$  are much lower than the corresponding observed values. With the exception of one line-of-sight, the CH absorption features appear to arise from interstellar clouds with  $n_{\text{H}} = 500 \text{ cm}^{-3}$ , although the corresponding values of observed  $N(\text{OH})$  far exceed the values predicted by these models.

Similar to the observed variation of  $N(\text{CH})$  with  $N(\text{H}_2)$ , the observed abundance of CH ( $X_{\text{CH}}$ ) is best explained by models with  $n_{\text{H}} = 500 \text{ cm}^{-3}$ . The observed median value of  $X_{\text{CH}}$  is  $3.55 \times 10^{-8}$ , with all the points lying between  $\sim 10^{-8}$  and  $10^{-7}$ .

We attempt to identify models that consistently explain both observed  $N(\text{OH})$  and  $N(\text{CH})$ , by comparing the  $N(\text{OH})/N(\text{CH})$  ratio as a function of  $N(\text{H}_2)$ . The results suggest that models with  $n_{\text{H}} = 100 \text{ cm}^{-3}$  and  $\chi = 0.1$ – $0.5 G_0$  reproduce the observed trends. However, on comparing the observed and model-predicted trends of  $N(\text{OH})$  and  $N(\text{CH})$  as functions of  $N(\text{H}_2)$  individually, it appears that absorption due to the two molecules must arise from clouds with densities different by as much as a factor of 10. The models with  $n_{\text{H}} = 50 \text{ cm}^{-3}$  and  $n_{\text{H}} = 500 \text{ cm}^{-3}$ , that respectively reproduce the observed  $N(\text{OH})$  and  $N(\text{CH})$  values separately, predict higher and lower values of  $N(\text{OH})/N(\text{CH})$  respectively. Mookerjee (2016) had reproduced the observed correlation between  $N(\text{OH})$  and  $N(\text{CH})$  by considering models with  $n_{\text{H}} = 500 \text{ cm}^{-3}$ ,  $\chi = 5 G_0$  and  $\zeta_{\text{CR}} = 10^{-14} \text{ s}^{-1}$ . However, as noted by the author, the observations cannot adequately constrain the three free parameters, viz.,  $n_{\text{H}}$ ,  $\chi$  and  $\zeta_{\text{CR}}$ .

## 5 DISCUSSION

The observed  $N(\text{OH})$ – $N(\text{H}_2)$  relation can be reproduced by CLOUDY-based FUV-illuminated diffuse cloud models with  $n_{\text{H}} = 50 \text{ cm}^{-3}$  and  $\chi = 1 G_0$ . This is consistent with the results obtained by Balashev et al. (2021) through their analytical and numerical models, though we note that they consider an ISRF equivalent to the Mathis field (Mathis et al. 1983) and apply a lower cosmic ray ionization rate of  $3 \times 10^{-17} \text{ s}^{-1}$ . While Balashev et al. (2021) probe only the OH chemistry in the diffuse ISM, we also investigate CH and  $\text{OH}^+$  through our models. The observed  $N(\text{CH})$  is reproduced only for molecular gas with densities of  $n_{\text{H}} = 500 \text{ cm}^{-3}$  irradiated by much weaker radiation fields, in contrast to the physical conditions deduced from the  $N(\text{OH})$  trends.

Fig. 3 shows various molecular abundance profiles obtained from CLOUDY models when radiation is incident on one side of the absorbing cloud. Using this, we further probe the molecular contributions from different regions within the absorbing cloud by tracing the changes in species abundances from the illuminated face of the cloud to the innermost shielded regions. When radiation is allowed to be incident on both sides of the cloud, similar abundance profiles are expected as a function of depth from each illuminated face of the absorber. For models with  $n_{\text{H}} = 50$  and  $100 \text{ cm}^{-3}$ , the OH abundance can be clearly seen as steadily increasing with  $N(\text{H}_2)$  and attaining a peak value of  $\sim 10^{-7}$  at  $N(\text{H}_2) \sim 5 \times 10^{19} \text{ cm}^{-2}$ . In comparison, when  $n_{\text{H}} = 500 \text{ cm}^{-3}$ , the OH abundance has values  $< 10^{-8}$  for  $N(\text{H}_2) < 10^{21} \text{ cm}^{-2}$ . Along similar lines, the models with lower den-

sities of 50 and  $100 \text{ cm}^{-3}$  show CH abundances slowly increasing with  $N(\text{H}_2)$ , but always being less than  $10^{-9}$  over the entire cloud. Only at the higher density of  $500 \text{ cm}^{-3}$  does the abundance increase to values of  $10^{-8}$  or more, for increasing values of  $N(\text{H}_2)$ .

We propose two possible reasons for the clear dichotomy in the derived densities of gas giving rise to the observed OH and CH column densities. The first possibility is that the OH and CH absorption arise from multiple clouds overlapping along the line of sight. If the velocities do not differ significantly, it would not be possible to distinctly identify the individual absorption lines at the resolution of the near-UV measurements. The second possibility is that both OH and CH absorption arise from the same spherical cloud with density gradients along the line-of-sight, such that OH is detected primarily in the outer layers of the cloud while the CH absorbing layers are seated deeper within the denser part of the cloud. Layered clouds with the molecular content increasing inward, akin to this latter possibility, were earlier invoked by Liszt & Lucas (1996) to explain the line profiles of OH and H I along the line of sight.

Fig. 3 also shows the abundance of  $\text{OH}^+$  predicted by the models. For models with  $n_{\text{H}} = 50 \text{ cm}^{-3}$  and  $\chi = 1 G_0$ , the abundance is found to increase up to  $\sim 10^{-8}$  for depths into the cloud corresponding to  $N(\text{H}_2) \sim 10^{19} \text{ cm}^{-2}$ , and then decreases with further increase in depth. For the higher-density models, the abundance of  $\text{OH}^+$  is much lower than a few times  $10^{-8}$ .

The models which reproduce the observed OH and CH column densities do not simultaneously predict consistent  $\text{OH}^+$  column densities. We infer that it is unlikely that the observed  $\text{OH}^+$  absorption features arise entirely due to the diffuse molecular clouds that give rise to OH absorption, or the denser clouds in which most of the CH exists. In fact, previous observations have suggested that  $\text{OH}^+$  resides primarily in clouds that are predominantly atomic (Neufeld et al. 2010; Indriolo et al. 2015), since  $\text{OH}^+$  is rapidly destroyed in reaction with  $\text{H}_2$ . It is possible that the observed  $\text{OH}^+$  column densities are indicative of high-energy inputs in the form of cosmic ray ionization or shocks. As there are only four  $\text{OH}^+$  detections with  $S/N > 3$  (two of these new), a detailed investigation of  $\text{OH}^+$  is beyond the scope of this paper.

## 6 SUMMARY

We have studied the correlation between OH and  $\text{H}_2$  column densities using NUV spectroscopic observations, to probe the suitability of OH as a surrogate for  $\text{H}_2$  in the diffuse interstellar clouds traced by these observations. To this effect, we have presented here a new determination of OH column densities for five sightlines along which direct estimates of  $\text{H}_2$  column densities are available, and have thereby increased the sightlines for which such data is available to seventeen. We have also included in our study, an additional nine sightlines with no reported  $\text{H}_2$  column densities, in order to explore the correlation between OH, CH and  $\text{OH}^+$ .

We find marginal correlation between the OH and  $\text{H}_2$  column density measurements at the 95 per cent confidence level, for  $N(\text{H}_2)$  in the range  $10^{20}$  to  $2 \times 10^{21} \text{ cm}^{-2}$ . We determine  $N(\text{OH})/N(\text{H}_2) = (1.32 \pm 0.15) \times 10^{-7}$ , which is substantially higher than previous estimates of the ratio. The observed  $N(\text{CH})$  shows significant correlation with the measured  $N(\text{H}_2)$ , as also with  $N(\text{OH})$ . We derive  $N(\text{OH})/N(\text{CH}) = 2.61 \pm 0.19$ , which is consistent with values found in literature (Liszt & Lucas 2002, and references therein). We conclude that while  $N(\text{OH})$  correlates well with  $N(\text{CH})$ , the correlation between  $N(\text{OH})$  and  $N(\text{H}_2)$  is not so clear from the near-UV measurements. Thus, to establish OH as a reliable tracer for  $\text{H}_2$ , it is

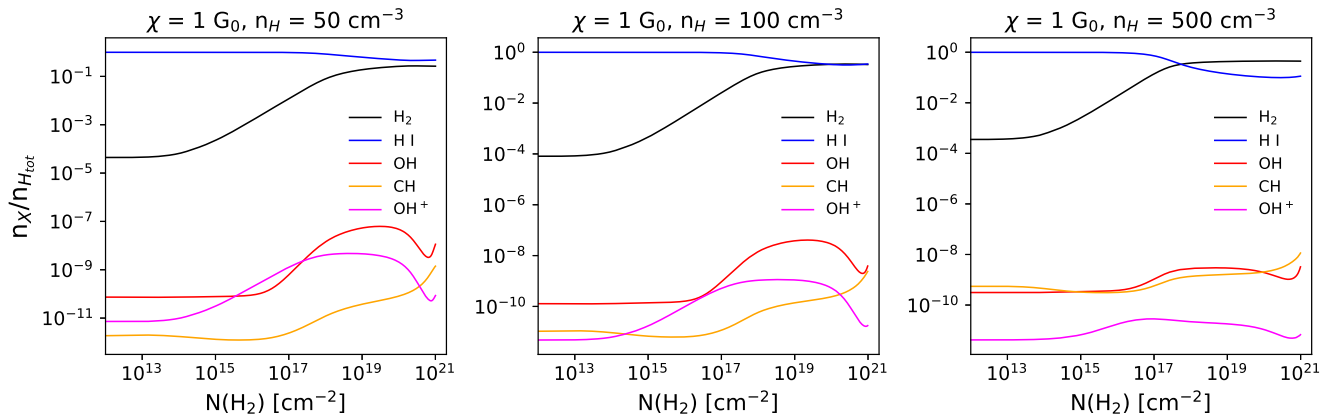


**Figure 3.** The plots indicate the variation in the densities of H I, H<sub>2</sub>, CH, OH and OH<sup>+</sup> species as a function of  $N(\text{H}_2)$ , that is effectively, as a function of depth when one face of the absorber is illuminated. The species density,  $n_X$ , is normalized using the corresponding total hydrogen density,  $n_{\text{Htot}}$ .

necessary to extend the study to more sightlines with direct measurement of  $N(\text{H}_2)$ , and also to higher values of  $N(\text{H}_2)$ .

Based on numerical models of photodissociation regions, we conclude that CH absorption arises from clouds with densities higher than those which produce OH absorption. We propose two possibilities to explain the situation – either CH and OH absorption arise from separate clouds of different densities lying along the same line-of-sight, or OH absorption arises from less dense portions of clouds whose denser regions are associated with CH absorption. We further infer that the observed OH<sup>+</sup> column densities cannot be explained by the physical conditions that give rise to OH and CH, thus suggesting that cosmic rays and/or other high-energy input mechanisms such as shocks may have a possible role in its origin.

## ACKNOWLEDGEMENTS

The authors thank the referee for insightful comments which helped improve the manuscript significantly. KR is grateful to TIFR for hospitality during academic visits related to this work. BM was supported by funding from the Department of Atomic Energy, Government of India, under Project Identification No. RTI 4002. This work makes use of spectra observed with the Ultraviolet & Visual Echelle Spectrograph on the Very Large Telescope at Cerro Paranal, Chile, and made available through the ESO science archive. Software used for data analysis: Python (Van Rossum & Drake 2009), PyRAF (Science Software Branch at STScI 2012), Numpy (Harris et al. 2020), Matplotlib (Hunter 2007), Scipy (Virtanen et al. 2020), Astropy (Astropy Collaboration et al. 2022), Pandas (pandas development team 2022).

## DATA AVAILABILITY

The results of this paper are based on data retrieved from the ESO telescope science archive, and numerical models generated using the code CLOUDY. No new observations have been carried out. Further details about the data analysis and/or numerical models can be made available on request to the authors.

## REFERENCES

- Ádámkóvics M., Blake G. A., McCall B. J., 2005, *ApJ*, **625**, 857  
 Adams W. S., 1941, *ApJ*, **93**, 11  
 Astropy Collaboration et al., 2022, *ApJ*, **935**, 167  
 Bacalla X. L., et al., 2019, *A&A*, **622**, A31  
 Balashev S. A., Gupta N., Kosenko D. N., 2021, *MNRAS*, **504**, 3797  
 Barriault L., Joncas G., Lockman F. J., Martin P. G., 2010, *MNRAS*, **407**, 2645  
 Bhatt N. H., Cami J., 2015, *ApJS*, **216**, 22  
 Black J. H., Dalgarno A., 1977, *ApJS*, **34**, 405  
 Bohlin R. C., Savage B. D., Drake J. F., 1978, *ApJ*, **224**, 132  
 Boissé P., Le Petit F., Rollinde E., Roueff E., Pineau des Forêts G., Andersson B. G., Gry C., Felenbok P., 2005, *A&A*, **429**, 509  
 Bolatto A. D., Wolfire M., Leroy A. K., 2013, *ARA&A*, **51**, 207  
 Cartledge S. I. B., Lauroesch J. T., Meyer D. M., Sofia U. J., 2004, *ApJ*, **613**, 1037  
 Chaffee F. H. J., Lutz B. L., 1977, *ApJ*, **213**, 394  
 Chalabaev A., Maillard J. P., 1983, *A&A*, **127**, 279  
 Chengalur J. N., de Bruyn A. G., Narasimha D., 1999, *A&A*, **343**, L79  
 Crutcher R. M., Watson W. D., 1976, *ApJ*, **203**, L123  
 Diplas A., Savage B. D., 1994, *ApJS*, **93**, 211  
 Dirks C., Meyer D. M., 2019, *ApJ*, **872**, 140  
 van Dishoeck E. F., Black J. H., 1986, *ApJS*, **62**, 109  
 Draine B. T., 2011, *Physics of the Interstellar and Intergalactic Medium*  
 Ferland G. J., et al., 2017, *Rev. Mex. Astron. Astrofis.*, **53**, 385  
 Fitzpatrick E. L., Massa D., 1990, *ApJS*, **72**, 163  
 Gerin M., Neufeld D. A., Goicoechea J. R., 2016, *ARA&A*, **54**, 181  
 Gupta N., Momjian E., Srianand R., Petitjean P., Noterdaeme P., Gyanchandani D., Sharma R., Kulkarni S., 2018, *ApJ*, **860**, L22  
 Gupta N., et al., 2021, *ApJ*, **907**, 11  
 Habing H. J., 1968, *Bull. Astron. Inst. Netherlands*, **19**, 421  
 Hanson M. M., Snow T. P., Black J. H., 1992, *ApJ*, **392**, 571  
 Harris C. R., et al., 2020, *Nature*, **585**, 357  
 Hodges J. N., Bittner D. M., Bernath P. F., 2018, *ApJ*, **855**, 21  
 Hollenbach D., Kaufman M. J., Neufeld D., Wolfire M., Goicoechea J. R., 2012, *ApJ*, **754**, 105  
 Hunter J. D., 2007, *Computing in Science & Engineering*, **9**, 90  
 Indriolo N., Geballe T. R., Oka T., McCall B. J., 2007, *ApJ*, **671**, 1736  
 Indriolo N., et al., 2015, *ApJ*, **800**, 40  
 Jacob A. M., et al., 2022, *ApJ*, **930**, 141  
 Kanekar N., Chengalur J. N., de Bruyn A. G., Narasimha D., 2003, *MNRAS*, **345**, L7  
 Krełowski J., Beletsky Y., Galazutdinov G. A., 2010, *ApJ*, **719**, L20  
 Lien D. J., 1984, *ApJ*, **284**, 578  
 Liszt H., 2003, *A&A*, **398**, 621

Liszt H., 2014, *ApJ*, **780**, 10  
 Liszt H., Lucas R., 1996, *A&A*, **314**, 917  
 Liszt H., Lucas R., 2002, *A&A*, **391**, 693  
 Magnani L., Siskind L., 1990, *ApJ*, **359**, 355  
 Marggraf O., Bluhm H., de Boer K. S., 2004, *A&A*, **416**, 251  
 Mathis J. S., Rumpl W., Nordsieck K. H., 1977, *ApJ*, **217**, 425  
 Mathis J. S., Mezger P. G., Panagia N., 1983, *A&A*, **128**, 212  
 Mattila K., 1986, *A&A*, **160**, 157  
 McKellar A., 1940, *PASP*, **52**, 312  
 Miville-Deschênes M.-A., Murray N., Lee E. J., 2017, *ApJ*, **834**, 57  
 Mookerjee B., 2016, *MNRAS*, **459**, 2822  
 Neufeld D. A., et al., 2010, *A&A*, **521**, L10  
 Nguyen H., et al., 2018, *ApJ*, **862**, 49  
 Pineda J. L., Langer W. D., Velusamy T., Goldsmith P. F., 2013, *A&A*, **554**, A103  
 Pineda J. L., Langer W. D., Goldsmith P. F., 2014, *A&A*, **570**, A121  
 Porras A. J., Federman S. R., Welty D. E., Ritchey A. M., 2014, *ApJ*, **781**, L8  
 Rachford B. L., et al., 2001, *ApJ*, **555**, 839  
 Rachford B. L., et al., 2002, *ApJ*, **577**, 221  
 Rachford B. L., et al., 2009, *ApJS*, **180**, 125  
 Rice J., 2018, PhD thesis, Univ. Toledo  
 van Rossum G., Drake F. L., 2009, Python 3 Reference Manual. CreateSpace, Scotts Valley, CA  
 Rugel M. R., et al., 2018, *A&A*, **618**, A159  
 Savage B. D., Bohlin R. C., Drake J. F., Budich W., 1977, *ApJ*, **216**, 291  
 Science Software Branch at STScI 2012, PyRAF: Python alternative for IRAF, Astrophysics Source Code Library, record ascl:1207.011 (ascl:1207.011)  
 Sheffer Y., Rogers M., Federman S. R., Lambert D. L., Gredel R., 2007, *ApJ*, **667**, 1002  
 Sheffer Y., Rogers M., Federman S. R., Abel N. P., Gredel R., Lambert D. L., Shaw G., 2008, *ApJ*, **687**, 1075  
 Shull J. M., Danforth C. W., Anderson K. L., 2021, *ApJ*, **911**, 55  
 Singh P. D., de Almeida A. A., 1980, *A&A*, **84**, 177  
 Snow T. P., McCall B. J., 2006, *ARA&A*, **44**, 367  
 Snow T. P., Black J. H., van Dishoeck E. F., Burks G., Crutcher R. M., Lutz B. L., Hanson M. M., Shuping R. Y., 1996, *ApJ*, **465**, 245  
 Swings P., Rosenfeld L., 1937, *ApJ*, **86**, 483  
 Tang N., et al., 2021, *ApJS*, **252**, 1  
 Tielens A. G. G. M., Hollenbach D., 1985, *ApJ*, **291**, 722  
 Velusamy T., Langer W. D., Goldsmith P. F., Pineda J. L., 2017, *ApJ*, **838**, 165  
 Virtanen P., et al., 2020, *Nature Methods*, **17**, 261  
 Wannier P., Andersson B. G., Penprase B. E., Federman S. R., 1999, *ApJ*, **510**, 291  
 Weinreb S., Barrett A. H., Meeks M. L., Henry J. C., 1963, *Nature*, **200**, 829  
 Welty D. E., Fowler J. R., 1992, *ApJ*, **393**, 193  
 Weselak T., 2019, *A&A*, **625**, A55  
 Weselak T., 2020, *Acta Astron.*, **70**, 301  
 Weselak T., Galazutdinov G., Beletsky Y., Krelowski J., 2009, *A&A*, **499**, 783  
 Weselak T., Galazutdinov G. A., Beletsky Y., Krelowski J., 2010, *MNRAS*, **402**, 1991  
 Whittet D. C. B., Goldsmith P. F., Pineda J. L., 2010, *ApJ*, **720**, 259  
 Wiesemeyer H., Güsten R., Heyminck S., Jacobs K., Menten K. M., Neufeld D. A., Requena-Torres M. A., Stutzki J., 2012, *A&A*, **542**, L7  
 Wiesemeyer H., et al., 2016, *A&A*, **585**, A76  
 Wolfire M. G., Tielens A. G. G. M., Hollenbach D., Kaufman M. J., 2008, *ApJ*, **680**, 384  
 Wolfire M. G., Hollenbach D., McKee C. F., 2010, *ApJ*, **716**, 1191  
 Wyrowski F., Menten K. M., Güsten R., Belloche A., 2010, *A&A*, **518**, A26  
 Xu D., Li D., Yue N., Goldsmith P. F., 2016, *ApJ*, **819**, 22  
 pandas development team T., 2022, pandas-dev/pandas: Pandas, doi:10.5281/zenodo.7093122, <https://doi.org/10.5281/zenodo.7093122>

**Table A1.** The diffuse Galactic sightlines in which OH absorption is detected in the present study

Source	Program ID	Galactic longitude (deg)	Galactic latitude (deg)
HD 23180	194.C-0833 <sup>a</sup>	160.3637	-17.7399
HD 41117	194.C-0833 <sup>a</sup>	189.6918	-0.8604
HD 46202	096.D-0008 <sup>b</sup>	206.3134	-2.0035
HD 62542	099.C-0637 <sup>c</sup>	255.9152	-9.2371
HD 73882	194.C-0833 <sup>a</sup>	260.1816	0.6431
HD 147683	194.C-0833 <sup>a</sup>	344.8565	10.0888
HD 147888	194.C-0833 <sup>a</sup>	353.6469	17.7092
HD 168076	194.C-0833 <sup>a</sup>	16.9371	0.8375
HD 179406	194.C-0833 <sup>a</sup>	28.2285	-8.3119
HD 203532	194.C-0833 <sup>a</sup>	309.4589	-31.7397

<sup>a</sup> PI: Cox, Nick, <sup>b</sup> PI: Hubrig, S., and <sup>c</sup> PI: Nieva, Maria-Fernanda

**Table A2.** Values of physical parameters considered in the models of diffuse interstellar clouds set up using CLOUDY

Physical parameter	Values adopted
Intensity of radiation field, $\chi$	0.05, 0.1, 0.5, 1, 2, 5, 10, 50, and 100 $G_0$
Total hydrogen density, $n_{\text{H}}$	50, 100, and 500 $\text{cm}^{-3}$
Metallicity	$Z_{\odot}$
Dust composition & abundance	ISM graphites and silicates
Cosmic ray ionization rate, $\zeta_{\text{CR}}$	$2 \times 10^{-16} \text{ s}^{-1}$
$N(\text{H}_2)$	20, 20.3, 20.5, 20.8, 21, and 21.3 ( $\log \text{cm}^{-2}$ )

## APPENDIX A: DETAILS OF UVES ARCHIVAL DATA AND CLOUDY MODELS

This paper has been typeset from a  $\text{\TeX}/\text{\LaTeX}$  file prepared by the author.